Journal of
Materials Chemistry C

COMMUNICATION

View Article Online
View Journal | View Issue

Open Access Article. Published on 19 November 2024. Downloaded on 07.04.2026 03:05:20.
This article is licensed under a Creative Commons Attribution 3.0 Unported Licence.

Check for updates

Cite this: *J. Mater. Chem. C*, 2024, **12**, 19035

Received 8th September 2024,
Accepted 13th November 2024

DOI: 10.1039/d4tc03865g

rsc.li/materials-c

Multifaceted classification and integration of time-varying complex signals using analog neuromorphic UV phototransistors†

Mohit Kumar,*[ab] Suwan Lee,[b] Hyunmin Dang[b] and Hyungtak Seo *[ab]

Human vision encompasses a sophisticated sensory and computational system capable of analyzing complex attributes such as color, intensity, duration, and nature (linear or non-linear) of light exposure, along with storing its termination details. Inspired by this, neuromorphic vision sensors have been developed to enhance real-time data processing and decision-making, surpassing conventional sensors. However, they fall short in accurate multifaceted classification, integration of complex and temporal patterns, and secure storage of outcomes, which are critical for precise monitoring, security, and forecasting of dynamic natural phenomena. Here, we present a generic approach to developing a neuromorphic optical sensor adept at multifaceted classification and integration of non-linear inputs. Leveraging the heterogeneity in UV response of two-dimensional electron gas-based thin-film transistors and robust persistent photoconductivity, our sensor precisely discriminates between 310, 365, and 395 nm wavelengths, mixed wavelengths, while tracking both the duration and termination of illumination. The sensor offers highly secure, in-sensor multibit data processing and storage with a high on/off ratio exceeding 10^7. Furthermore, it adeptly handles real-time dynamic sensing, integration, and revelation of both linear and non-linear optical inputs as dictated by differential equations, including logistic maps, and is capable of monitoring complex dynamic phenomena such as those caused by water vortices.

1. Introduction

Light illumination, such as ultraviolet (UV) radiation, is fundamental to life and pivotal to various technologies.[1,2] However, the effectiveness of these technologies hinges on the accurate measurement of illumination parameters, like intensity, duration, and wavelengths (single or mixed).[1–3] Even minimal discrepancies in these parameters during processes can cause significant changes, influencing outcomes in critical areas of application; for instance, protecting human health against harmful UV exposure, catalyzing advancements in water purification, chemical synthesis, environmental monitoring, and optical communications.[1,2,4–7] Therefore, real-time, and precise measurement of these crucial parameters is essential for optimizing the performance of these applications.[8] Despite the critical nature of these measurements, however, traditional UV sensing technologies are often expensive and frequently fall short, especially when dealing with the variable and non-linear nature of UV radiation, such as in solar radiation, which limits their functionality.[4,9,10] Furthermore, once UV exposure is terminated, these devices typically fail to provide essential data, such as the duration of exposure and the exact timing of its cessation.[4,10] This underscores the necessity for a sophisticated and energy efficient new type of UV photosensor that can accurately measure these parameters. Developing such a photosensor would significantly enhance the accuracy and effectiveness of applications reliant on precise UV measurements.

In this scenario, neuromorphic optical sensors could effectively address the multifaceted classification and integration of time-varying complex dynamic signals by dynamically responding to illumination conditions such as distinct wavelengths and intensities, along with detailed data storage.[11–15] The term ''multifaceted classification'' in this study refers to the device's ability to differentiate between various input characteristics, such as wavelength, intensity, and exposure duration, of the UV signals. This capability allows the sensor to analyze and classify complex signal patterns across multiple parameters simultaneously, which is essential for real-time monitoring in dynamic environments. Reported neuromorphic systems demonstrate superior capabilities in processing optical data promptly and with reduced energy consumption compared to traditional sensors.[16–19] However, for these systems to achieve their full potential in critical applications, it is imperative not only to

---

[a] *Department of Energy Systems Research, Ajou University, Suwon, 16499, Republic of Korea. E-mail: mohitiopb@ajou.ac.kr, hseo@ajou.ac.kr*

[b] *Department of Materials Science and Engineering, Ajou University, Suwon, 16499, Republic of Korea*

† Electronic supplementary information (ESI) available. See DOI: **https://doi.org/10.1039/d4tc03865g**

Open Access Article. Published on 19 November 2024. Downloaded on 07.04.2026 03:05:20. This article is licensed under a Creative Commons Attribution 3.0 Unported Licence.

measure accurately but also to ensure the security of the collected data. This is particularly crucial in domains where the integrity of sensitive information is paramount.[14,20,21] The vulnerability of these systems to unauthorized access poses significant risks. The integration of advanced security features with precise UV measurement capabilities addresses both the accuracy and security requirements of critical applications. This advancement ensures the integrity and confidentiality of sensitive data while maintaining adaptability to changing conditions. Therefore, the development of such sophisticated UV photosensors within neuromorphic systems would significantly enhance the accuracy, effectiveness, and security of applications reliant on precise UV measurements.

To address these gaps, we developed neuromorphic optical sensors capable of precise discrimination and real-time integration of intensity, as well as securely storing the optical multibit digital and analogue information. By leveraging the heterogeneity in UV response of two-dimensional electron gas-based thin-film transistors and robust persistent photoconductivity, our sensor not only accurately discriminates between 310, 365, and 395 nm wavelengths, including mixed wavelengths, but also tracks both the duration and termination of illumination. Moreover, it supports highly secure, in-sensor multibit data processing and storage with an exceptional on/off ratio exceeding 10^7. The sensor's ability to integrate both linear and non-linear optical inputs in real-time, guided by differential equations such as logistic maps, makes it adept at monitoring complex dynamic patterns such as dynamic of water vortexes. This study presents an innovative neuromorphic optical sensor that integrates multifaceted classification with secure, dynamic storage of complex UV signals, surpassing the capabilities of traditional sensors. Leveraging persistent photoconductivity within a two-dimensional electron gas-based thin-film transistor platform, our approach enables real-time, in-sensor classification and integration of both linear and non-linear UV inputs. This adaptability supports advanced monitoring and secure data processing, with applications in fields that demand high sensitivity and secure data handling for analyzing complex dynamic patterns, such as natural phenomena.

2. Results and discussion

Fig. 1a illustrates the schematic layout of the devices, featuring four thin-film transistors (TFTs) with the same channel width (W) of 10 μm but varying channel lengths (L) of 50, 100, 150, and 200 μm. Fig. 1b presents a complete single chip comprising sixteen devices with different W (ranging from 50 to 200 μm) and L from 5 to 40 μm. This intentional variation in W and L introduces a unique randomness ideal for highly secure optical data storage and classification tasks. The diverse configurations of W and L mimic biological variability, making it challenging to reproduce one set of devices from another, thereby offering highly secure on-chip sensing and classification.[22,23] Each TFT responds uniquely to specific intensities and/or wavelengths of optical input, resulting in a unique output pattern for a given input. This unique pattern allows for accurate prediction and classification of inputs based on measured responses. Indeed, our proposed concept leverages this variability in response, providing a versatile approach to classify not only optical inputs but potentially other types of inputs as well, such as gases, thereby broadening the application scope of our approach.

To validate the device fabrication, transmission electron microscopy (TEM) was employed. Fig. 1c shows the cross-sectional TEM image of a device, highlighting the ultrathin (~3 nm) indium oxide (In_2O_3) layer on top of a 10 nm aluminum oxide (Al_2O_3) layer, with a bottom gate and top source/drain (S/D) made of gold/titanium (Au/Ti). The magnified view in Fig. 1d further emphasizes the uniformity and thickness of the In_2O_3 layer. Additionally, the composition variation across these layers was confirmed by energy-dispersive X-ray (EDS) mapping, as shown in Fig. S1 (ESI†). Furthermore, the growth and composition of the In_2O_3 layer were confirmed by X-ray photoelectron spectroscopy (XPS), as detailed in Fig. S2 (ESI†).

The growth of In_2O_3 on top of Al_2O_3 can lead to defect modulation doping, resulting in the formation of a 2-dimensional electron gas-like conducting channel. Therefore, to understand the critical role of oxygen environment, spatially resolved electron energy loss spectroscopy (EELS) spectra in the range of 500 to 600 eV were mapped across the yellow dotted line in Fig. 1e. The spectra from Al_2O_3 to In_2O_3, plotted in Fig. 1f, elucidate the O–K edge transitions across the Al_2O_3/In_2O_3 heterostructure. The EELS map in Fig. 1e highlights three distinct regions: the Al_2O_3 layer, the interface, and In_2O_3. Variations in energy loss indicate differences in elemental composition and electronic structure between these regions. For instance, the interface region exhibits a gradient in energy loss, indicative of a transition zone with mixed bonding environments, as marked by the red arrow in Fig. 1e.

The corresponding EELS spectra in Fig. 1f provide detailed information about electronic transitions at various depths through the interface, showing a prominent peak around 535 eV corresponding to the O–K edge.[24] This peak, associated with electronic transitions from the O 1s core level to unoccupied states above the Fermi level, varies in intensity and position with depth, reflecting changes in the oxygen bonding environment. In the Al_2O_3 region, the O–K edge peak appears at higher energies (~535.3 eV), indicative of Al–O bonds, while in the In_2O_3 region, the peak shifts to lower energies (~533 eV), characteristic of In–O bonds.[25] The interface displays a continuous shift in the O–K edge peak, confirming a mixed Al–O and In–O bonding environment.[24–26] Peak analysis of the O–K edge position, shown in Fig. 1g, reveals the depth profile across the interface. The shift from ~535 eV in Al_2O_3 to ~533 eV in In_2O_3 underscores the different electronic structures and bonding states of these materials.[25,26] The gradual change in peak position within the interface suggests intermixing of Al and In atoms, leading to an interfacial layer with unique electronic properties, likely due to the formation of sub-stoichiometric compounds and defects.[25,27] Indeed, the peak value at interface was close to 532 eV, which is an indicative of 2D metallic layer imbedded in the interfacial oxides to provide a 2D electron gas.

This journal is © The Royal Society of Chemistry 2024

Open Access Article. Published on 19 November 2024. Downloaded on 07.04.2026 03:05:20. This article is licensed under a Creative Commons Attribution 3.0 Unported Licence.

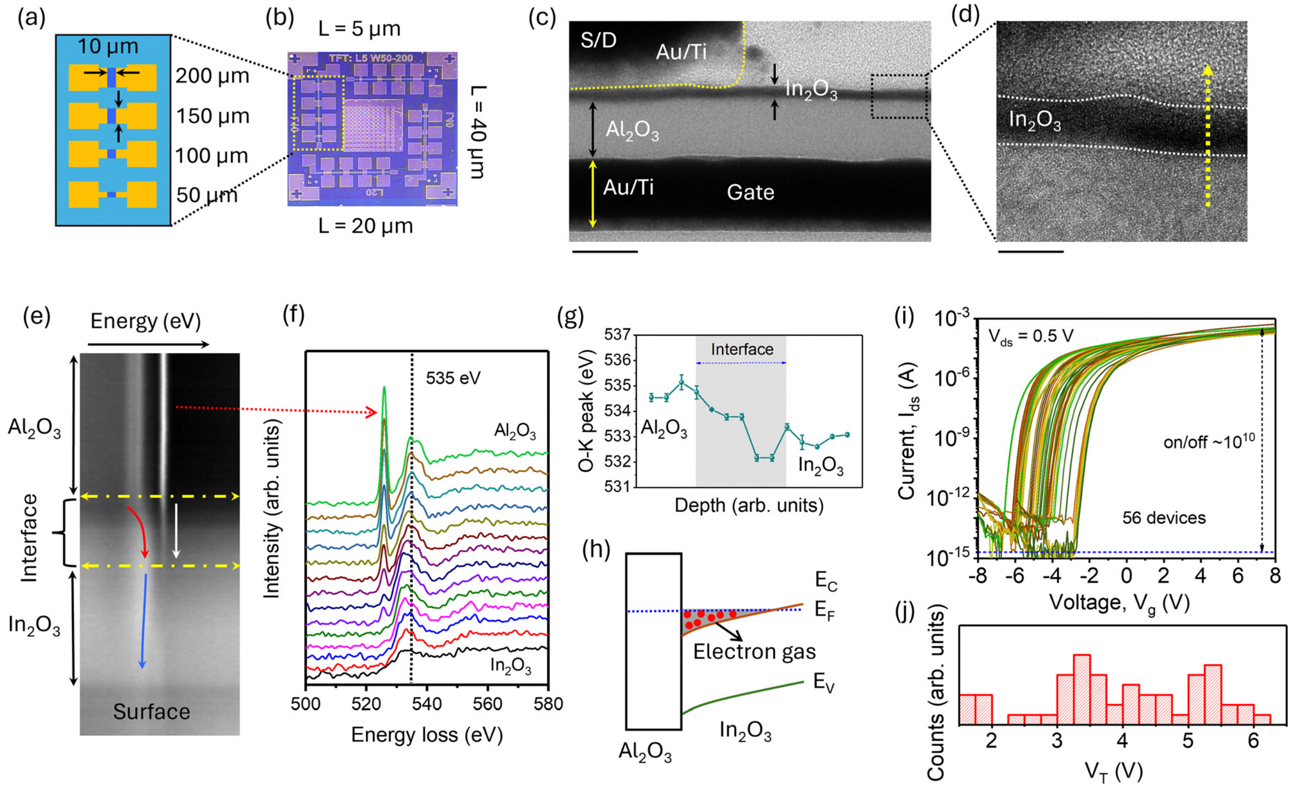

Fig. 1 Fabrication and analysis of indium oxide (In_2O_3) thin film transistors (TFTs). (a) Schematic diagram of the TFT device layout, showing different channel lengths ranging from 50 to 200 μm with a fixed channel width of 10 μm. (b) Optical microscope image of the fabricated sixteen TFTs on a chip, having different *L* and *W* values. (c) Cross-sectional transmission electron microscopy (TEM) image of the TFT structure, highlighting the layers of Au/Ti (S/D, source/drain), Al_2O_3 (gate dielectric), and In_2O_3 (channel). The scale bar indicates 10 nm. (d) High-resolution TEM image magnifying at the interface between the Al_2O_3 and the In_2O_3 channel. The scale bar indicates 3 nm. (e) Electron energy loss spectroscopy (EELS) map across the interface of Al_2O_3 and In_2O_3, providing insight into the oxygen environment change. (f) EELS spectra collected at various points across the Al_2O_3/In_2O_3 interface, with a noticeable peak close to 535 eV indicating the presence of oxygen. (g) Depth profile of the peak value of O–K energy across the Al_2O_3/In_2O_3, revealing a transition region with distinct chemical states of oxygen in both materials. (h) Band diagram representation illustrating the formation of an electron gas at the Al_2O_3/In_2O_3 interface due to band alignment. (i) Transfer characteristics of the TFTs, showing the drain current (I_{ds}) as a function of gate voltage (V_g) at a drain voltage (V_{ds}) of 0.5 V. The on/off current ratio is approximately 10^{10}, indicating excellent switching performance. (j) Histogram of threshold voltages (V_T) for the TFTs, demonstrating the broad range of variation.

These interfacial defect states can significantly impact carrier density through defect modulation doping, leading to the formation of quasi-static 2D electron density.[27]

In line with the EELS spectra, the XPS spectra also confirm the presence of oxygen defects (see Fig. S2, ESI†). Based on these spectra and literature, we draw the band alignment at the In_2O_3/Al_2O_3 interface, as illustrated in Fig. 1h.[25] This diagram highlights the presence of a two-dimensional electron gas (2DEG) at the interface.[25] The conduction band (E_C) and valence band (E_V) offsets between Al_2O_3 and In_2O_3 create a band alignment such that the conduction band shifts below the Fermi level (E_F), leading to electron accumulation and the formation of the 2DEG.

Having the characterization, the electrical characterization of the TFTs was performed, focusing on the source-to-drain current (I_{ds}) as a function of gate voltage (V_g). Measurements were taken from 56 randomly selected TFTs with varied channel widths and lengths from 6 chips on a single platform. The I_{ds}–V_g curves reveal that the current remains around $\sim 10^{-12}$ A under negative gate voltages, escalating to approximately 10^{-3} A as V_g progresses towards positive biases, as presented in Fig. 1i. This behavior is indicative of n-type TFTs,[28,29] demonstrating a remarkable on/off current ratio of 10^{10}, which signifies the high performance of these devices. Such a high on/off ratio can be attributed to the atomic layer deposition grown In_2O_3 and Al_2O_3, which provides a smooth interface between them.

Furthermore, the threshold voltage (V_T)—defined as the gate voltage at which I_{ds} begins to increase significantly—exhibits a broad distribution. For deeper insight, V_T was determined from the sqrt(I_{ds}) *versus* V_g plots (refer to Fig. S3, ESI†), which elucidates the extensive distribution of V_T values ranging from 1.5 to 6.5 V, as illustrated in Fig. 1j. This extensive variation in V_T does not exhibit a straightforward correlation with the channel dimensions, suggesting that the primary cause is the intrinsic heterogeneity induced by the fabrication process. To assess this heterogeneity, Kelvin probe force microscopy (KPFM) was utilized, and the contact potential difference (V_{cpd}) was measured, showing clear variation between different devices (see Fig. S4, ESI†).[30] This indicates the presence of In_2O_3 channel

Open Access Article. Published on 19 November 2024. Downloaded on 07.04.2026 03:05:20.
This article is licensed under a Creative Commons Attribution 3.0 Unported Licence.

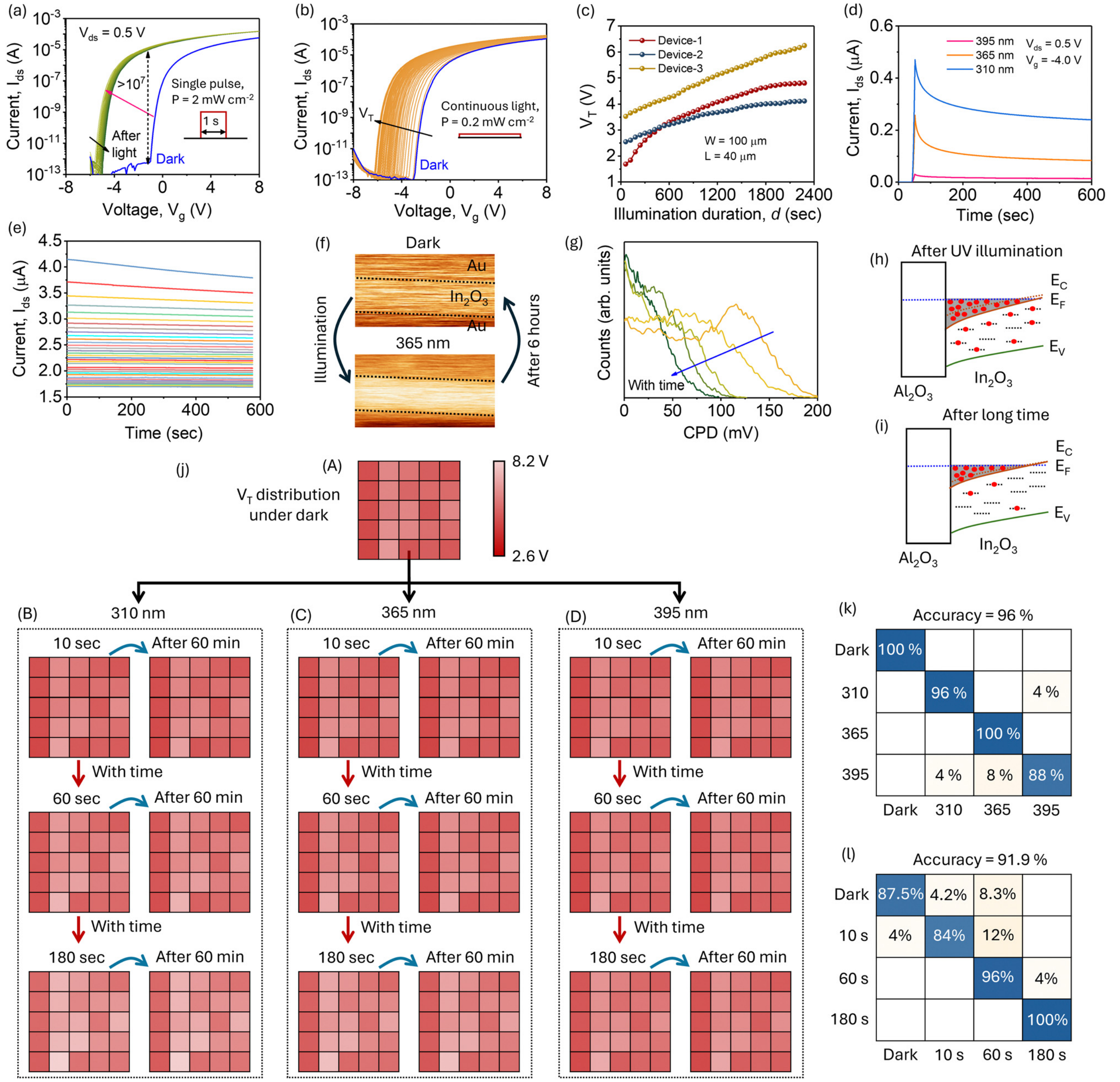

(k) Accuracy = 96 %

	Dark	310	365	395
Dark	100 %			
310		96 %		4 %
365			100 %	
395		4 %	8 %	88 %

(l) Accuracy = 91.9 %

	Dark	10 s	60 s	180 s
Dark	87.5%	4.2%	8.3%	
10 s	4%	84%	12%	
60 s			96%	4%
180 s				100%

Fig. 2 Photoresponse and variability of TFTs. (a) Transfer characteristics of a TFT under dark conditions and after illumination with a single light pulse (λ = 365 nm, intensity = 2 mW cm^{-2}). The inset shows the shape of the light pulse. (b) Transfer characteristics of a TFT under continuous illumination (0.2 mW cm^{-2}) compared to dark conditions, highlighting the persistent effect of light on the device performance. The gradual change of V_T is depicted by black arrow. (c) Variations in V_T with illumination duration for three different TFTs, showing the device-to-device variation. (d) Transient response of a TFT for three different wavelengths (310 nm, 365 nm, and 395 nm), indicating wavelength-dependent behavior. (e) The I_{ds} behavior for number of cycles after illuminating the TFT for a short pulse of UV (λ = 365 nm, d = 10 s), showing dynamic multilevel current. (f) The contact potential difference (V_{cpd}) maps of the TFT before (top image) and after illumination (bottom image) of UV. Black arrows show the change from dark-to-illuminated condition. (g) Histogram of the V_{cpd} values measured after hours of illumination, showing a decrease over time, which suggests photo-induced changes in surface potential. Energy band diagrams of Al_2O_3/In_2O_3 interface (h) after UV illumination and (i) after waiting for long time, showing dynamic change of alignment. (j) (A) Distribution of V_T under dark conditions for 25 TFTs, showing the variance across several measurements. Variation of V_T after illumination after illumination with (B) λ = 310, (C) 365, and (D) 395 nm for d = 10, 60, and 180 seconds. The corresponding right distribution shows the V_T variation for the same devices after 60 min, displaying the effect of wavelength and exposure time on device performance. The confusion matrix for the (k) wavelength and (l), illumination duration classification, showing the accuracy of the classification.

heterogeneity. Therefore, this broad spectrum of V_T not only highlights the impact of fabrication-induced variability but also underscores the potential for optimizing device performance through controlled heterogeneity. It is worth noting that although the chip shows device-to-device variation, the devices exhibit high stability over numerous cycles, as depicted in Fig. S5 (ESI†).

This journal is © The Royal Society of Chemistry 2024

Open Access Article. Published on 19 November 2024. Downloaded on 07.04.2026 03:05:20.
This article is licensed under a Creative Commons Attribution 3.0 Unported Licence.

To exploit the inherent heterogeneity for optoelectronic applications, we examined the photoactive characteristics of the TFTs. Fig. 2a illustrates the I_{ds} *versus* V_g behavior of a specific TFT both in the dark (blue curve) and after exposure to a short UV optical pulse (λ = 365 nm, intensity, $P \sim 2$ mW cm^{-2}, duration, $d \sim 1$ second, green curves, see inset). Under dark conditions, V_T was recorded at −1.4 V; however, post-illumination, V_T shifted significantly to −6.2 V, indicating enhanced n-type behavior, likely due to a substantial increase in electron density. Importantly, this notable V_T shift under post-illumination is not transient; V_T does not immediately revert to its pre-illumination value (blue curve) once the light is removed. Instead, it gradually and slowly returns towards the dark V_T, suggesting that a single optical pulse effectively modulates the n-type nature of the TFT. As marked by the black arrow in Fig. 2a, this gradual return to the original V_T indicates persistent photocurrent, highlighting the device's potential for optical information storage. Furthermore, the on/off current ratio below V_T (*i.e.*, −2.0 V) found $\sim 10^7$, as depicted by the vertical blue arrow in Fig. 2a. This high on/off ratio is critical for achieving multilevel photocurrent states through precise control of conductance states *via* optical means, which is useful for optical memory storage devices, indicating the robustness of the 2DEG to sense the photons.

In the pursuit of achieving multilevel photocurrent states through precise optical control of electronic states, we analyzed the I_{ds} *versus* V_g behavior of a TFT under continuous UV illumination (λ = 365 nm) at a low intensity of 0.2 mW cm^{-2}. Notably, under these conditions, both the I_{ds} curves and V_T gradually shifted towards more negative biases. For example, as illustrated in Fig. 2b, the V_T for this particular TFT was −3.2 V under dark conditions (blue curve), and it gradually shifted to −6.4 V under UV illumination, confirming the presence of controllable multilevel states by selecting an appropriate duration of the illumination. The gradual shift in V_T demonstrates the device's capability to achieve and maintain intermediate states, which is crucial for advanced data sensing and processing applications. This behavior underscores the device's sensitivity to optical stimuli and its suitability for applications requiring precise control over electronic states, as shown in Fig. S6 (ESI†). Furthermore, the ability to modulate the electronic properties of the TFT through continuous light exposure highlights its potential for optoelectronic memory devices and other applications that benefit from light-induced state changes.

It is noteworthy that the V_T under dark conditions varies from device to device, and their photoresponses can also be distinctly different. To investigate this, we measured the change in V_T under continuous UV illumination (λ = 365 nm, P = 0.2 mW cm^{-2}) for three TFTs, each with the same W of 100 μm and L of 40 μm. As illustrated in Fig. 2c, V_T gradually changes for all three devices, but the variation is markedly distinct. For example, in Device-1, the magnitude of V_T shifts from 1.7 V to 4.12 V and then saturates. In contrast, Device-3 exhibits a V_T change from 3.5 V to 6.2 V without saturation within the measurement time of 2400 seconds. Similarly, V_T for Device-2 shows distinct behavior compared to Devices 1 and 3. This outcome is significant because it enables precise prediction of illumination duration and intensity for this specific λ of 365 nm. Devices with reproducible responses across different devices do not offer this advantage; for them, achieving a specific V_T at a given duration under an intensity of 0.2 mW cm^{-2} might require shorter illumination times with higher intensities, complicating accurate predictions. Therefore, the unique, non-reproducible responses observed here highlight the potential for developing advanced optoelectronic devices tailored for specific photoresponse characteristics. The device-to-device variability observed in our neuromorphic optical sensor primarily arises from intrinsic heterogeneity during fabrication, resulting in controlled and reproducible variations within specified tolerance ranges. Notably, these variations do not compromise critical device functions, such as the high on/off ratio and persistent photoconductivity, which remain consistent across devices. This controlled variability aligns with neuromorphic design principles, where slight differences across devices can enhance multifaceted classification, much like variability in biological systems.

To further explore the device characteristics, we tested the transient response of an In_2O_3-based TFT under three different UV wavelengths: 310, 365, and 395 nm, as shown in Fig. 2d. The device exhibited significant photocurrent (I_p) generation, with the magnitude of I_p depending on the illuminated λ. For instance, the I_p value for λ of 310 nm (P = 2 mW cm^{-2}) was 0.46 μA, whereas it was 0.21 μA and 0.04 μA for the λ of 365 nm and 395 nm, respectively. This distinct, wavelength-dependent response indicates that our devices can be used not only to detect illumination intensity and duration but also to classify different UV wavelengths. Additionally, I_{ds} decay gradually after the illumination is removed, and importantly, this gradual I_{ds} change is independent of the illumination wavelength. This can be attributed to intrinsic device properties, such as the distribution of defects.[31] The gradual change in I_{ds} is akin to the short-term memory (STM) observed in biological synapses, suggesting potential applications in neuromorphic vision systems.[19,32,33] To further investigate the persistent photocurrent, I_{ds} was measured over 600 seconds for multiple cycles, as shown in Fig. 2e. After removing the illumination, I_{ds} gradually decay, shifting to lower levels with each cycle. This behavior, similar to the observed V_T shifts, confirms the presence of persistent photocurrent. The gradual and well-separated current levels are crucial for storing dynamic multilevel data.

To understand the persistent I_p nature, KPFM was employed. The contact potential difference (V_{cpd}) was measured at the In_2O_3 layer before and after UV illumination, including the top electrodes, as shown in Fig. S7 (ESI†). The V_{cpd} of the top electrodes was intentionally measured, as being metal (*i.e.*, Au/Ti), V_{cpd} does not change from dark to illuminated conditions, providing a stable reference point to understand the relative dynamic variation in the In_2O_3 layer. The V_{cpd} maps of the device before and after UV illumination (λ = 365 nm, 2 mW cm^{-2}, d = 10 seconds) are shown in the top and bottom images of Fig. 2f, respectively. Notably, the V_{cpd} contrast changes significantly after illumination and gradually returns to its dark level over time, as illustrated in the

Open Access Article. Published on 19 November 2024. Downloaded on 07.04.2026 03:05:20.
This article is licensed under a Creative Commons Attribution 3.0 Unported Licence.

accompanying image in Fig. S7 (ESI†). Further, the effective change of the V_{cpd} after illumination varies from device to device, indicating that the dynamic photoresponse varies notably (Fig. S7, ESI†). This shift in V_{cpd} post-illumination indicates the presence of trapped electrons, and its gradual decay can be attributed to electron detrapping.[34] To clarify the working mechanism of our neuromorphic optical sensor, we provide a schematic diagram (Fig. S7, ESI†) illustrating the underlying processes. Upon UV illumination, a two-dimensional electron gas (2DEG) forms at the In_2O_3/Al_2O_3 interface, enabling persistent photoconductivity as electrons become trapped at the interface. This trapped charge facilitates a dynamic memory effect, where the photocurrent gradually decays over time due to electron detrapping. The device's capability to store varying levels of photocurrent based on wavelength and exposure time underpins its functionality for UV classification and secure, in-sensor data storage. Indeed, the CPD measurements serve as a diagnostic tool for analyzing surface potential variability in our devices, which affects the threshold voltage (V_{T}) and overall device performance. The observed differences, shown in Fig. S4 and S7 (ESI†), reflect heterogeneity in the In_2O_3 layer due to fabrication variations. Such heterogeneity introduces controlled device-to-device variability without impeding core functions (*e.g.*, high on/off ratio, persistent photoconductivity). Instead, this variability enhances neuromorphic classification capabilities, as each device exhibits a unique response profile. This variability also benefits secure key applications by making each device a unique identifier, thus supporting highly secure data storage and authentication.

For better clarity, the distribution of V_{cpd} from the time-dependent maps is plotted in Fig. 2g, revealing notable features. For instance, V_{cpd} exhibits a broad distribution with a peak value close to 120 mV, which shifts back towards the original dark value over time, indicating detrapping. These measurements reveal that UV illumination enhances the effective electron concentration in the In_2O_3 layer, leading to n-type behavior and dynamic variability in I_{ds} and V_{T}. This persistence and gradual decay of V_{cpd} highlight the underlying mechanisms of charge trapping and detrapping.

The observed persistent I_{p} behavior can be illustrated schematically in Fig. 2h and i, which show the band alignment and electron dynamics at the Al_2O_3/In_2O_3 interface immediately after UV illumination and after an extended period, respectively.[21,35] Upon UV illumination, as depicted in Fig. 2h, there is a significant increase in electron density at the interface, enhancing the n-type behavior of the 2DEG. Over time, as shown in Fig. 2i, the electron density gradually decreases as trapped electrons are detrapped, leading to a reduction in the n-type behavior of 2DEG. The persistence and gradual decay of electron density at the interface, observed through V_{cpd} measurements and the shifts in V_{T} and I_{ds}, highlights the dynamic charge trapping and detrapping mechanisms in the device. Indeed, the presence of 2DEG at the In_2O_3/Al_2O_3 interface provides a unique platform for multilevel dynamic memory with controllable V_{T} values, depending on the illumination duration and/or intensity.

Following the important information provided by the device-to-device variability, we confirmed the ability of our approach to classify the λ, P, and d of illumination. Twenty-five devices from three chips on a single platform were subjected to different wavelengths (310, 365, and 395 nm) for varying durations. Before these measurements, we ensured all devices returned to their baseline dark levels by keeping them under dark conditions for one week. The distribution of the V_{T} from these devices under dark conditions is displayed in panel (A) of Fig. 2j along with the original magnitude in Fig. S8 (ESI†), indicating a broad range. Subsequently, the V_{T} maps after illuminating these devices for 10, 60, and 180 seconds at 310, 365, and 395 nm are depicted from top to bottom in panels (B), (C), and (D) of Fig. 2j along with their magnitudes in Fig. S9 and S10 (ESI†). The images on the right in each panel show the V_{T} distribution 60 minutes post-illumination.

Notably, V_{T} varies significantly across different illumination conditions; however, discerning these differences solely by visual inspection of the panels can be challenging, which is beneficial to store the secure optical data. Quantitatively, the shift in V_{T} was most pronounced at the 310 nm wavelength, reflecting the higher energy associated with shorter wavelengths. For example, after 180 seconds of illumination at 310 nm, the average V_{T} shifted from its initial dark level by approximately 2.0 V. In contrast, the 395 nm wavelength induced a smaller V_{T} shift, around 0.5 V under the same conditions, highlighting the lower energy impact of longer wavelengths. Moreover, the persistence of these V_{T} shifts over time underscores the devices' capacity to retain optical information. The gradual reversion to the dark V_{T} level, as observed in the 60-minute post-illumination maps, suggests these devices' potential to function as dynamic memory elements. This persistence and distinct response under various conditions facilitate the classification of input UV information based on observed V_{T} shifts, unlike devices with uniform V_{T} where similar responses might be induced by different wavelengths and intensities. These findings highlight the potential of using these TFTs in applications that require wavelength classification and intensity detection, including sophisticated data processing and memory storage capabilities.

To discriminate the output from various devices based on the illumination parameters (λ, P, and d), we employed an optimized neural network approach using MATLAB, as detailed in the experimental section. This method was designed to accurately classify the conditions under which these devices were tested, focusing on the wavelengths and durations of UV exposure; however, it can be extended to other parameters such as intensity. The classification results are presented in the confusion matrices shown in Fig. 2k and l.

The confusion matrix in Fig. 2k illustrates the neural network's performance in distinguishing between different wavelengths (310, 365, and 395 nm) compared to a baseline dark condition. Remarkably, the neural network achieved an overall classification accuracy of 96%. Specifically, the network demonstrated perfect classification accuracy for the 365 nm wavelength (100%) and high accuracy for the 310 nm and 395 nm

This journal is © The Royal Society of Chemistry 2024

Open Access Article. Published on 19 November 2024. Downloaded on 07.04.2026 03:05:20.
This article is licensed under a Creative Commons Attribution 3.0 Unported Licence.

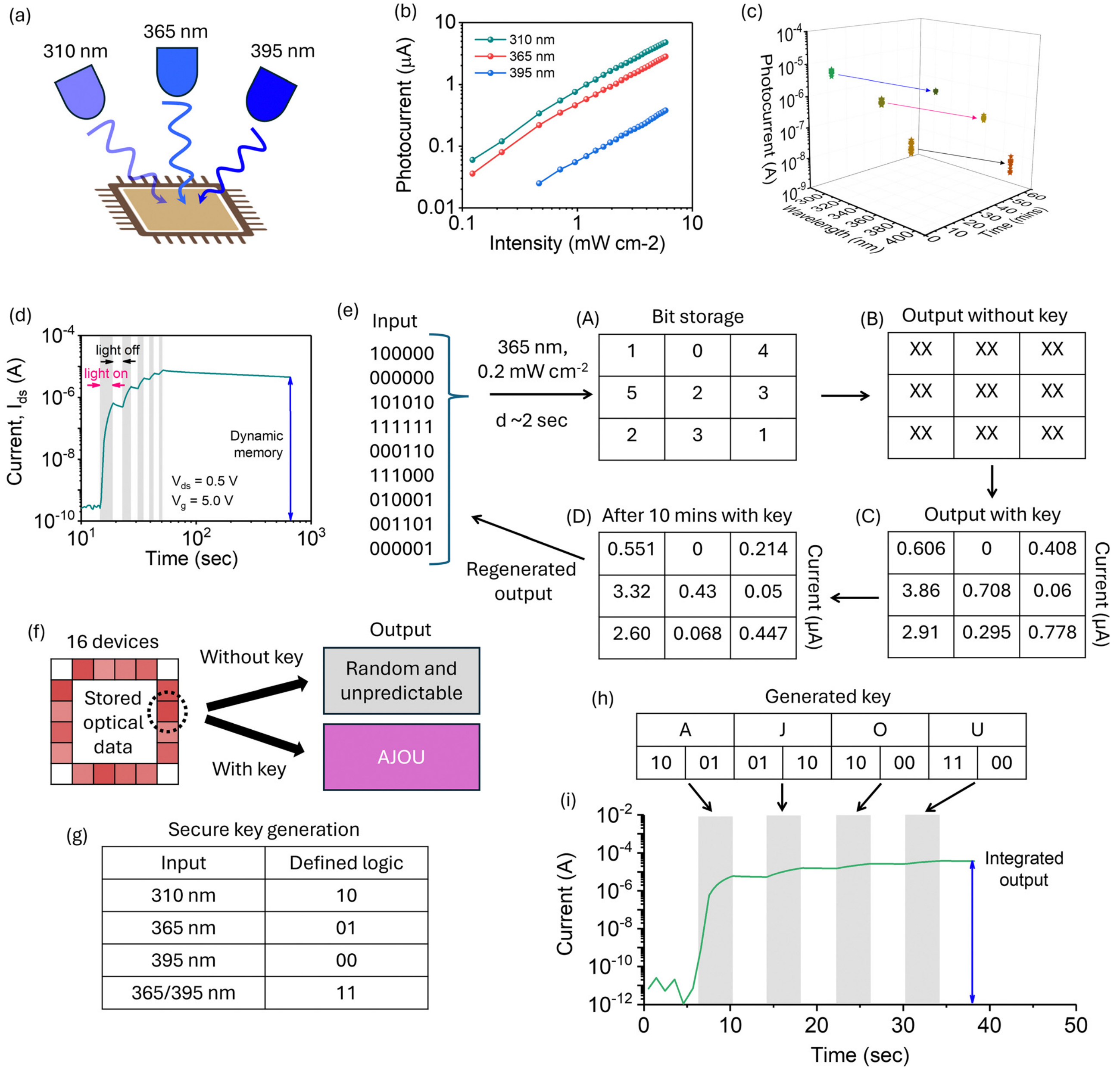

Fig. 3 Secure optical information encoding and decoding using thin film transistors (TFTs) with multi-wavelength UV light. (a) Schematic of the device setup showing a thin film transistor (TFT) illuminated by three different wavelengths of light (310 nm, 365 nm, and 395 nm) simultaneously. (b) Graph showing the photocurrent of the TFT at three different wavelengths as a function of light intensity (from 0.1 to 10 mW cm^{-2}). Each line represents a distinct wavelength, illustrating the device's sensitivity and response range. (c) 3D plot of the photocurrent as a function of light intensity and wavelength for multiple devices. Each point represents a different combination of intensity and wavelength, showing variations in device performance. (d) Transient response of the device illustrating the dynamic response and memory effect. The graph shows the current decay over time after illumination is turned off, highlighting the persistent photoconductivity of the device. (e) Data encoding and decoding process: nine binary optical input pulses (d ∼ 2 s) in a random manner were selected and shown from top to bottom. (A) Showing the nine TFTs and illuminated sequence of input. (B) Output reading without the key, resulting in indecipherable data ('XX' represents unreadable or random data). (C) Output reading with the key, showing the correctly deciphered current levels corresponding to the input data. (D) Regenerated output after 10 minutes with the key, demonstrating data retention and retrieval capabilities. (f) Diagram illustrating data storage and retrieval in a system of 16 devices, comparing the outputs with and without the cryptographic key, emphasizing security and data integrity. Out of these only one TFT was selected to store the data, as shown by black circle, while all others are illuminated with random optical inputs. (g) Logic diagram for secure key generation using the defined wavelength inputs of wavelength of 310 nm, 365 nm, 395 nm, and dual-wavelength 365/395 nm, which are assigned to 10, 01, 00, and 11, respectively. The combination enables complex encoding schemes. (h) Example of a generated cryptographic key based on the logic inputs, demonstrating how specific patterns of light can be used to create secure keys. (i) Graph showing the temporal response of current under coded light exposure, followed by the integrated output signal, which is significant for decoding the transmitted information.

Open Access Article. Published on 19 November 2024. Downloaded on 07.04.2026 03:05:20.
This article is licensed under a Creative Commons Attribution 3.0 Unported Licence.

wavelengths, with minor misclassifications primarily between closely related conditions. Additionally, the confusion matrix in Fig. 2l details the network's performance in classifying based on exposure duration (10, 60, and 180 seconds) against the dark baseline. The neural network achieved an overall accuracy of 91.9%. It perfectly identified the 180-second exposure scenario (100% accuracy) and showed substantial accuracy for the 60-second exposures (96%). The slightly lower accuracy for the 10-second exposures (84%) is likely due to the minimal changes in device behavior over such short durations, presenting a more challenging classification task. Furthermore, if the device is illuminated with unknown parameters (λ, P, and d), the output response, such as the V_T distribution from the devices, can be used to predict the illumination parameters. This capability offers unique and valuable information for storing optical data in a non-volatile manner.

To harness the ability of our devices to differentiate wavelength and illumination duration, we applied these features in practical applications. Fig. 3a depicts the interaction of UV light at three specific wavelengths—310 nm, 365 nm, and 395 nm—with our TFT devices. This setup enables the simultaneous or individual illumination at these wavelengths, allowing us to evaluate how different wavelengths variably influence the TFTs' response, thereby affecting their performance and functionality. The intensity-dependent I_p response of the devices to these UV wavelengths was quantitatively analyzed and is presented on a logarithmic scale in Fig. 3b. The data illustrates a pronounced λ-dependent I_p response. Notably, at $\lambda = 310$ nm, the devices exhibit the highest I_p across all intensity levels. By contrast, the response at $\lambda = 365$ nm, though slightly diminished, remains substantial. At $\lambda = 395$ nm—approaching the visible spectrum—the I_p is markedly lower, indicating decreased sensitivity with increasing wavelength. These findings are pivotal for refining TFT device applications in UV sensing, photodetection, and optoelectronics, where customized wavelength sensitivity is essential.

To understand the dynamic behavior of the I_p, we measured the value of the photocurrent immediately after illumination and again after 60 minutes with ($V > V_T$). The three-dimensional plot in Fig. 3c provides a comprehensive quantitative analysis of the I_p response in 18 In_2O_3-based TFT devices, mapped against time and λ on logarithmic scales. At a λ of 310 nm, the devices exhibit I_p values of approximately 10^{-5} A, which gradually decrease to around 10^{-6} A over 60 minutes. This slow decay indicates a strong and sustained response to UV light. In comparison, at $\lambda = 365$ nm, the devices show a significant but less pronounced persistent photocurrent effect, with initial I_p values around 10^{-6} A, declining to about 10^{-7} A over the same period. At $\lambda = 395$ nm, the initial I_p is around 10^{-7} A, with a more rapid decrease to 10^{-8} A within 60 minutes, highlighting a faster recovery and reduced sensitivity to this longer UV wavelength, as shown in Fig. S11 (ESI†).

Driven by the persistent photocurrent, the device exhibits a dynamic response to an increasing number of light pulses.[33,35,36] Fig. 3d illustrates this dynamic response (*i.e.*, I_{ds} at V_{ds} of 0.5 V and V_g of 5 V) and the memory behavior of a specific In_2O_3 TFT device under multiple light pulses (λ = 365 nm, P = 2 mW cm^{-2}). Initially, with the light off, the current remains at a low level of $\sim 10^{-10}$ A, indicating the off state of the TFT. Upon illumination, the I_{ds} sharply increases, reaching a peak value around 10^{-5} A. During the light-off periods, as indicated by the gray backgrounds in Fig. 3d, the I_{ds} gradually decay, demonstrating the device's persistence in response and STM-like behavior. Notably, the I_{ds} increases with subsequent optical pulses of the same parameters, although the increase is not uniform across all pulses. For example, the I_{ds} stabilizes within the range of 10^{-6} A for the second and subsequent pulses. Furthermore, the I_{ds} decays gradually and slowly over time, which can be attributed to the persistent photocurrent effect.[35,37] Even after the light is turned off, the current remains at a high level, around 10^{-6} A, for an extended period (>600 seconds), demonstrating the device's dynamic memory capabilities.

The dynamic response varies among devices, exhibiting behavior akin to an artificial synapse.[19,38] Such pulse-dependent dynamic responses are crucial for data processing and secure data storage applications. While conventional PUFs are known for their robustness and are resistant to cloning, they typically generate a static key that does not change over time or in response to different conditions.[31] This static nature can be a limitation in dynamic environments where adaptable security measures are essential. In contrast, neuromorphic-based PUFs offer a more dynamic alternative by incorporating the learning and adaptability features of neuromorphic circuits. This capability enhances security through unique, non-reproducible keys tailored to each session and adapts to changing conditions, providing a robust and versatile security mechanism for neuromorphic vision technologies. Despite the potential, the direct implementation of these adaptable security features into neuromorphic vision sensors remains largely unexplored and undeveloped.

Therefore, to explore the first potential application of this device-to-device variability, along with dynamic photoresponse, we implemented our devices for highly secure data storage. Nine TFTs were randomly selected from sixteen devices on a chip, and optical pulses in different sequences were illuminated on these devices, as shown by the input in Fig. 3e. Here, '0' indicates the LED off condition and '1' corresponds to the LED on condition ($\lambda \sim 365$ nm, 0.2 mW cm^{-2}, $d \sim 2$ s). The applied multibit sequences for these nine TFTs are shown in panel (A) of Fig. 3e. Due to device-to-device variation and without knowledge of the key—which includes accurate information of the illuminated TFTs and their V_T values—it is almost impossible to reveal the stored information. Indeed, random, and unpredictable values could be measured without the accurate key, as indicated by 'XX' in panel (B).

However, when the correct key is provided, as shown in panel (C), the stored current values are revealed. For successful data retrieval, it is necessary to know not only the distribution of the V_T values but also the illuminated λ and intensity. Following the detailed information of the key and the method of data storage, the retrieved currents, which range from 0 to

Open Access Article. Published on 19 November 2024. Downloaded on 07.04.2026 03:05:20.
This article is licensed under a Creative Commons Attribution 3.0 Unported Licence.

3.86 μA, can be used to accurately classify the stored bits. Additionally, it is worth noting that the current from individual TFTs changes dynamically, and thus, once the data is stored, it changes over time. For instance, after 10 minutes with the key (panel D), the current values exhibit slight decay due to persistent photocurrent characteristics. Therefore, additional information on the I_p decay behavior of individual TFTs is essential to regenerate the stored bit information. The ability to encode, securely store, and accurately retrieve data over time underscores the suitability of these devices for advanced optoelectronic memory applications.

Additionally, highly secure data can be stored in a selective device; for instance, a particular device is marked by the black circle in Fig. 3f. This figure illustrates the secure data storage and retrieval process using 16 TFT devices on a chip. Optical data is stored in these devices, and the retrieval process can yield either random and unpredictable values without the correct key or the intended output when the correct key is applied. In this example, the stored output spells 'AJOU' when the key is correctly used. Fig. 3g outlines the secure key generation process. The key is defined by the input wavelength: 310 nm corresponds to the logic '10', 365 nm to '01', 395 nm to '00', and a combination of 365/395 nm to '11'. In our study, we use two distinct binary encoding schemes. For LED illumination status in multibit data storage, we use '0' to indicate the LED off condition and '1' for the LED on condition ($\lambda \sim$365 nm, 0.2 mW cm^{-2}, $d \sim$2 s). For secure key generation (Fig. 3g), we assign binary pairs to specific UV wavelengths, such as '10' for 310 nm and '01' for 365 nm. This wavelength-based encoding allows for unique key generation, separate from the simple on/off logic used for multibit storage. These defined logics are crucial for accurately accessing the stored data. A secure key can be generated by selecting random arrangements of UV wavelengths. For example, 310, 365, and 395 nm can also be assigned to '11', '10', and '01', respectively. These bits can then be rearranged to generate the key for a specific message.

Fig. 3h presents the generated key for the specific example. The letters 'A', 'J', 'O', and 'U' are encoded with the key sequences '10', '01', '01', and '10', respectively. This key must be used to retrieve the stored data accurately. For example, the letters 'AJOU' are designed by selecting the bits 1001, 0110, 1000, and 1100, as depicted in the table in Fig. 3h. Fig. 3i shows the dynamic current response of the devices over time with the key applied. The current, plotted on a logarithmic scale, initially shows a low level around 10^{-12} A. Upon application of the correct key (indicated by the gray bars), the current increases significantly, stabilizing around 10^{-6} A. The LEDs were illuminated on all sixteen TFTs, and the response was measured for the specifically selected TFT, as shown in Fig. 3i. This integrated output confirms the successful retrieval of the stored data, as indicated by the steady current levels maintained over the measurement period. These results demonstrate the robustness and effectiveness of using In_2O_3 TFT devices for secure optical data storage and retrieval. The ability to generate secure keys based on specific UV wavelengths and the accurate retrieval of stored data with gradual change over time highlights the potential for advanced optoelectronic memory applications. The secure key generation process leverages specific binary codes assigned to UV wavelengths (*e.g.*, 310 nm as "10" and 365 nm as "01"). These codes are combined into a unique sequence that serves as an encryption key for multibit data storage. To retrieve data, the device must be illuminated with the correct sequence of wavelengths in the designated order. Only when the precise key sequence is applied will the device output a readable photocurrent pattern, enabling secure data retrieval. In Fig. 3i, we illustrate this process: the correct key sequence, when applied, activates the device, resulting in a stable photocurrent output that corresponds to the stored data. Without the correct key, the photocurrent remains inconsistent or random, preventing unauthorized access to the data. This method ensures a robust, secure data storage solution within the device.

Our neuromorphic optical sensor leverages persistent photoconductivity at the two-dimensional electron gas (2DEG) interface of In_2O_3/Al_2O_3 to achieve multibit data storage. Upon UV illumination, the sensor's photocurrent levels are modulated by the wavelength and duration of exposure, resulting in discrete, persistent current states that represent multibit data. These current levels are retained within the device even after illumination stops, due to slow detrapping processes that maintain charge over extended periods. For secure key applications, device-to-device variability plays a crucial role by introducing unique, non-reproducible responses in each device. This controlled variability allows each sensor to function as a unique identifier, where only a specific input (or "key") will generate the correct current output from a designated device. Key generation relies on assigning specific UV wavelengths to binary logic states (*e.g.*, 310 nm as '10' and 365 nm as '01'), enabling a sequence that can only be accurately decoded by a device with matching stored parameters. This variability-driven encoding process ensures that, without the correct key—knowledge of precise wavelengths and exposure durations—unauthorized access produces incorrect or random outputs, adding a robust layer of security.

The slow response driven by persistent photocurrent in our phototransistors extends their utility beyond secure data storage, making them ideal for systems that involve integration processes. Fig. 4a illustrates the schematic representation of a phototransistor-based system used for various applications under analogue illumination, including solar radiation, chemical reactions, water purification, and biological systems.[9,10] The effective intensity of transmitted UV light changes due to interactions within the non-linear system, enabling our phototransistors to capture real-time fluctuations. This slow response allows our devices to solve complex phenomenon by integrating light exposure over time, thereby enhancing computational capabilities. Indeed, our approach offers a new platform for understanding natural phenomena.

As a demonstration, TFT devices were illuminated by varying the UV (λ = 365 nm) intensity in three different ways: linear, harmonic, and damped harmonic. Fig. 4b–d present the varying light intensity behavior (top image), measured photoresponse of

Open Access Article. Published on 19 November 2024. Downloaded on 07.04.2026 03:05:20.
This article is licensed under a Creative Commons Attribution 3.0 Unported Licence.

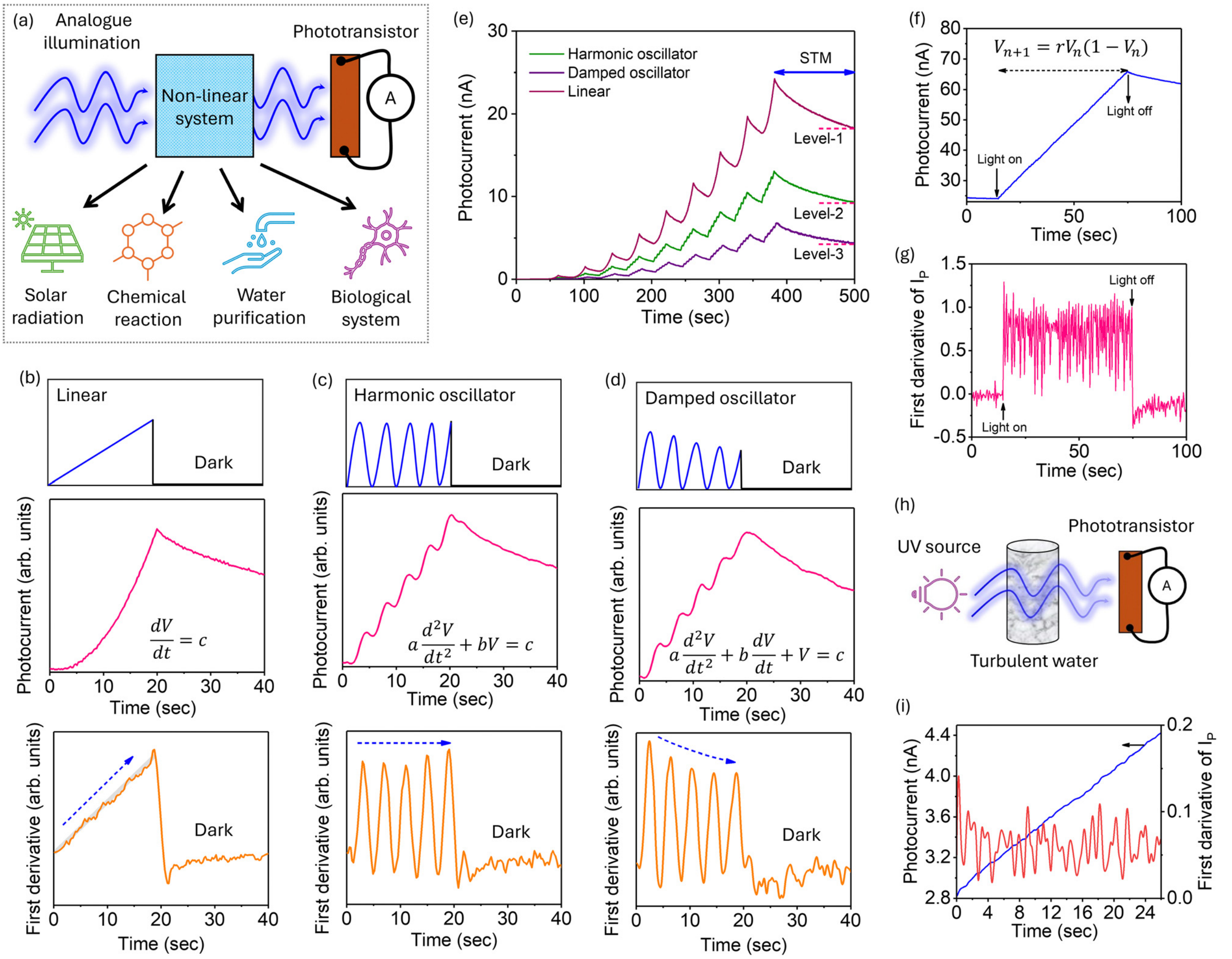

Fig. 4 Dynamic and integrated response of the TFTs and under different illumination as per mathematical models. (a) Schematic representation of the proposed utilization of the TFTs under analog illumination and its applications in various fields such as solar radiation management, chemical reactions, water purification, and biological systems. (b) Response of the TFT under liner change of the light intensity. Top: Illustrates the linear increase in illumination intensity. Middle: Response of the TFT, Bottom: First derivative of photocurrent, representing a linear response over time. (c) Harmonic oscillator model of illumination: Top: Depicts periodic oscillations of LED typical of a harmonic oscillator. Middle: Time graph showing photocurrent oscillations. Bottom: First derivative of photocurrent, showing harmonic oscillations, indicating the input pattern. (d) Response of TFT with damped oscillator model: Top: Shows LED illumination as per dampened oscillations reducing over time. Middle: Time graph displaying a decreasing amplitude in photocurrent. Bottom: First derivative of photocurrent, indicative of a damped oscillatory response. The corresponding equations are shown in the inset of middle images. The blue dotted arrows in (b), (c), and (d) indicate the behavior of the first derivative of I_P, which matches closely with the inputs. (e) Graph comparing the photocurrent generation under the illumination of LED for three different ways harmonic oscillator, damped oscillator, and linear. The STM is for short-term memory. The current decay after a time of 500 s is shown by level-1, 2, and 3. (f) The dynamic photocurrent of the TFT as per the illumination intensity change as per logistic growth model, showing the integrated light intensity as per logistic growth behavior. (g) First derivative of photocurrent as a function of time calculated from (f), showing rapid fluctuations, reflecting the dynamic response of the system to changing light conditions. (h) The experimental setup, in which the transmitted light through disturbed water was illuminated to the TFT. (i) Combined graph showing photocurrent and its first derivative over time with overlaid experimental data.

TFT (middle image) and first derivative of the photocurrent (bottom image) under these different types of illumination inputs, represented by specific differential equations. Indeed, these figures illustrate how the devices react to varied light conditions.

For instance, in Fig. 4b, the TFT device is subjected to a linear light intensity input, described by the differential equation $\frac{\mathrm{d}V}{\mathrm{d}t} = c$, where c is a constant and V is the applied voltage to the LED. The UV intensity increases linearly over time and is then turned off after 20 seconds (see top image). The I_p follows the illuminating intensity and increases gradually, demonstrating the integrating nature of the input optical information. It is worth noting that the I_p changes non-linearly even with linear illumination, which can be attributed to the integration nature of our TFT. In fact, the I_p at time t integrates with the I_p at $t + 1$ second, showing a gradual change, as depicted in the bottom panel of Fig. 4b. Since the rate change, for instance, $\mathrm{d}I_\mathrm{p}/\mathrm{d}t$, depicts the variation, and thus, first derivative (bottom image) shows the actual behavior of the I_p change, which varies linearly.

Open Access Article. Published on 19 November 2024. Downloaded on 07.04.2026 03:05:20. This article is licensed under a Creative Commons Attribution 3.0 Unported Licence.

Similarly, in Fig. 4c, the I_p response to the harmonic oscillator illumination is governed by the differential equation $a\frac{d^2V}{dt^2} + V = c$, where a is a constant. The top image displays the oscillatory nature of the input UV illumination, while the middle image shows the corresponding I_p response. The I_p exhibits periodic peaks corresponding to the oscillations of the input light, indicating the device's ability to track non-linear changes in light intensity. Additionally, the gradual increase in I_p suggests the integration capability of the TFT for non-linear illumination. This periodic response reflects the dynamic adaptability of the TFT device, crucial for applications requiring precise temporal modulation and integration of light. Indeed, the harmonic nature of the illumination can be revealed clearly by the first derivative (see bottom image). It is important to mention that the first derivative of I_p closely matches the behavior of the input. Thus, even with the slow and analog response of our devices, it is capable of revealing the true nature of the inputs.

Further, Fig. 4d explores the response of our TFT to a damped harmonic oscillator input, where the light intensity oscillates with decreasing amplitude over time, according to the differential equation: $a\frac{d^2V}{dt^2} + b\frac{dV}{dt} = c$, where b is the damping term (see top image). The measured I_p due to damped oscillatory input illumination is depicted in the middle image of Fig. 4d. The I_p initially follows the oscillatory pattern but gradually diminishes as the oscillations are dampened, showcasing a complex interplay between persistence and damping effects. This behavior indicates the device's potential for applications where damped responses are essential, such as in adaptive sensing. The nature of damping UV input is clearly seen from the first derivative (see bottom image). Indeed, our TFT can sense both linear and non-linear UV information and integrate it over time. Whereas the first derivative can be used to sense the real-time variation of the inputs. These observations of the TFT photoresponses under varied illumination conditions highlight the devices' versatility and robustness for both linear and non-linear illumination. In Fig. 4, panels (b), (c), and (d) use arbitrary units to emphasize the comparative nature of the response variations, focusing on proportional changes rather than absolute values. Panel (i), however, provides an absolute measurement with actual units and a scale bar, offering precise quantification of the response for applications requiring specific value references.

The integration of both linear and non-linear input illuminations allows the device to store memory in a distinguishable manner. Fig. 4e illustrates the dynamic response of the TFT device when exposed to three types of UV patterns—linear, harmonic, and damped—each repeated ten times. The I_p changes gradually for all three types of illuminations, but the magnitude of the I_p is distinct for each pattern, demonstrating the device's ability to differentiate between various types of analogue light inputs. For linear illumination, the maximum I_p reaches 24.3 nA, showing a consistent increase with each illumination. In contrast, harmonic illumination results in a lower maximum I_p of 13 nA, characterized by periodic peaks that reflect the oscillatory nature of the input. Damped illumination produces an even lower maximum I_p of 6.8 nA, with the photocurrent gradually diminishing over time, highlighting the device's response to decreasing amplitude oscillations. Furthermore, the current decay behavior leads to distinct memory levels at the 500-second mark, identified as Level-1, Level-2, and Level-3 in Fig. 4e. These levels correspond to the different types of illumination inputs, with linear illumination showing the highest persistent current, followed by harmonic and damped oscillations. These observations indicate that the TFT device not only integrates varying input illuminations but also retains memory of the illumination type and intensity.

Beyond integrating simple UV light patterns, the TFT can also respond to more complex behaviors.[39,40] For instance, the TFT device is illuminated according to a logistic map function, represented by the equation $V_{n+1} = rV_n(1 - V_n)$, where r is a constant and V_n represents the normalized light intensity at step n. Fig. 4f and g illustrate the I_p response of TFT devices under a nonlinear logistic map input and its first derivative. These figures provide insights into the device's performance under sophisticated light modulation. As shown in Fig. 4f, the I_p rises steadily from 30 nA, following the logistic map pattern, and reaches a peak of approximately 70 nA before the light is turned off. The first derivative of I_p, depicted in Fig. 4g, shows complex variations, which can be attributed to the intricate behavior of the logistic map pattern. The device integrates the input according to this complex pattern, highlighting dynamic behaviors and the derivative of the I_p over time. This demonstrates the device's ability to sense and integrate complex input information. Furthermore, after the light is turned off, the photocurrent exhibits a gradual decay, demonstrating the device's memory behavior. This memory retention and ability to follow complex input patterns underscore the potential of TFT devices for advanced optoelectronic applications, where sophisticated light modulation and integration are required.

Moreover, Fig. 4h illustrates the practical application of our TFT device in capturing the I_p response to UV light modulated by disturbed water, which was shaken to simulate dynamic conditions. The measured I_p, starting at $\sim$2.8 nA and steadily increasing to around 4.4 nA over 24 seconds (see blue curve), indicating the device's ability to integrate and accumulate light exposure, as shown in Fig. 4i. The red line shows the first derivative of I_p, reflecting the rate of change in the photocurrent. The oscillatory behavior of the derivative, superimposed on the steadily increasing I_p, highlights the dynamic variations in light intensity caused by the water disturbance. The theoretical behavior of such behavior can be modeled by the equation $I_p(t) = I_0 + A.e^{-\gamma t}\cos(\omega t + \varphi)$, where the terms describe the linear growth and damped oscillations in the I_p. However, real natural systems are more complex, and the feedback from our system provides valuable insights to understand these complexities. This practical demonstration showcases the TFT device's dual functionality: integrating overall light exposure while capturing rapid intensity fluctuations due to environmental disturbances, making it highly suitable for advanced

Open Access Article. Published on 19 November 2024. Downloaded on 07.04.2026 03:05:20.
This article is licensed under a Creative Commons Attribution 3.0 Unported Licence.

optoelectronic applications such as adaptive sensing and environmental monitoring. It is worth to mention that the device-to-device variability is crucial here since that can be applied to classification of λ, P, d, using the same concept as in Fig. 2j. In the turbulent water scenario shown in Fig. 4, scattered and attenuated UV waves mimic real-world environmental conditions, enabling dynamic inputs for the neuromorphic sensor. This analog illumination model finds applications in fields such as solar radiation management, where monitoring scattered solar UV components informs atmospheric and radiation studies. In chemical reactions, analog UV control optimizes photochemical processes by fine-tuning reaction conditions. For water purification, scattered UV illumination helps assess the efficacy of UV disinfection in varying water conditions, ensuring adaptability to environmental changes. In biological systems, analog UV illumination replicates natural light conditions, allowing for controlled studies of UV effects on cellular processes. Our approach enhances computational capabilities by facilitating in-sensor data processing, enabling each device to classify and integrate UV signals in real-time based on persistent photoconductivity and multibit data storage. This functionality allows the sensor to independently perform complex data processing tasks, enhancing efficiency by reducing reliance on external computation. Additionally, while UV response and signal processing are the main focus, the sensor's adaptive capability can extend to dynamic environmental monitoring. For instance, the sensor could monitor complex, time-varying phenomena like water vortices by responding to fluctuating UV signals. This adaptability highlights the device's broader potential in applications that demand real-time, non-linear data integration.

Our neuromorphic optical sensor offers versatile applications in fields that demand dynamic and sensitive UV signal processing. Key examples include environmental monitoring, where the sensor's high sensitivity to UV intensity and wavelength allows for tracking and predicting changes in atmospheric conditions. Additionally, the secure, in-sensor data storage capability of our device makes it ideal for secure data storage and retrieval, a valuable asset in cybersecurity applications. Furthermore, the sensor's ability to integrate and classify dynamic UV inputs in real time makes it suitable for adaptive sensing in optoelectronic systems, supporting efficient monitoring of complex dynamic phenomena, such as water purification processes and solar radiation analysis.

3. Conclusion

In conclusion, our research introduces a conceptually new neuromorphic optical sensor that revolutionizes UV light classification and dynamic optical event sensing. By leveraging the unique properties of two-dimensional electron gas-based thin-film transistors, this sensor achieves unparalleled accuracy and security in multibit data processing and storage. Its ability to seamlessly integrate and process both linear and non-linear optical inputs in real-time, guided by differential equations, makes it an indispensable tool for monitoring complex dynamic patterns. The versatility and robustness demonstrated in handling intricate signals, such as those from disturbed water, highlight its potential for diverse real-world applications. This advancement marks a significant leap forward in the fields of optoelectronics and adaptive sensing technologies, paving the way for next-generation neuromorphic sensors with broad, impactful applications in UV dosimetry and beyond.

4. Experimental section

4.1. Device fabrication

The fabrication of the device involves a bottom gate structure, utilizing a silicon (Si) substrate coated with a thermally grown 300 nm silicon dioxide (SiO_2) layer. The substrate underwent a cleaning process using acetone, isopropyl alcohol (IPA), and deionized water (DIW), each for 5 minutes, followed by RCA cleaning to ensure thorough cleanliness. For the gate electrode, a titanium/gold (Ti/Au) layer with thicknesses of 5 nm and 20 nm respectively was deposited using an electron-beam evaporator *via* the lift-off method. The gate oxide consists of a 20 nm layer of aluminum oxide (Al_2O_3) deposited at 200 °C through thermal atomic layer deposition (ALD) using trimethylaluminum (TMA) as the precursor. The growth per cycle (GPC) achieved for Al_2O_3 was 1.25 Å per cycle. After the deposition of Al_2O_3, photolithography was performed, followed by wet etching using a phosphoric acid and DIW dilution solution. Subsequently, the indium oxide (In_2O_3) channel layer was deposited using thermal ALD with dimethylaminoethanol (DADI) as the precursor. The channel layer was deposited to a thickness of 5 nm at a processing temperature of 175 °C, achieving a GPC of 0.35 Å per cycle. Post-deposition, another photolithography process was executed, and the etching was performed using an oxalic acid and DIW dilution solution. Finally, the source/drain (S/D) electrodes, consisting of 10 nm Ti and 40 nm Au, were deposited using the same electron-beam evaporator and the lift-off method. This process resulted in the fabrication of a transistor with a bottom gate structure and a minimum line width of 5 μm.

4.2. Characterization

Transmission electron microscopy (TEM), energy dispersive X-ray spectroscopy (EDS), and electron energy loss spectroscopy (EELS): all required TEM, EDS, and EELS measurements were conducted using a JEOL JEM-2100 F transmission electron microscope. Cross-section TEM samples were prepared using focus ion-beam to examine the structural and compositional characteristics at the nanoscale. EDS was employed to determine the elemental composition and distribution within the samples, while EELS provided information on the electronic structure and chemical bonding of the elements present.

X-ray photoelectron spectroscopy (XPS). The composition analysis of the samples was carried out using X-ray photoelectron spectroscopy (XPS). A Thermo Fisher Scientific NEXSA system equipped with an Al Kα (1486.6 eV) source was used

Open Access Article. Published on 19 November 2024. Downloaded on 07.04.2026 03:05:20.
This article is licensed under a Creative Commons Attribution 3.0 Unported Licence.

for this purpose. The X-ray spot size was set to 400 μm to ensure adequate spatial resolution and surface sensitivity.

4.3. Electrical characterization

Electrical characterization of the devices was performed using a Keithley 4200 source meter. To ensure accurate measurements, the experiments were conducted on a vibration isolation table to minimize external disturbances. The Keithley 4200 source meter provided precise control and measurement of current–voltage (*I*–*V*) characteristics, enabling detailed analysis of the electrical properties of the devices.

LED Illumination. For the illumination experiments, UV LEDs of different wavelengths were utilized. Specifically, LEDs with wavelengths of 310 ± 10 nm, 365 ± 10 nm, and 395 ± 10 nm were used. An Arduino microcontroller was programmed to control the illumination patterns and intensities of the LEDs, allowing for precise and repeatable experimental conditions. The influence of different wavelengths on the samples was systematically studied under controlled illumination conditions. For measurements involving water, DI water was used to study the effects of turbulence and other dynamic phenomena on the surface potential.

Kelvin probe force microscopy (KPFM). KPFM measurements were conducted using an Asylum Research system (Oxford Instruments). KPFM was used to map the surface potential and work function variations across the sample surface.

4.4. MATLAB for classification

Data classification was performed using MATLAB. The classification learner app was utilized to train and optimize a support vector machine (SVM) model. The kernel function used in the SVM model was Gaussian, and model hyperparameters were optimized to achieve the best classification performance. This analysis helped in identifying patterns and correlations in the experimental data. To classify wavelength and exposure duration, we employed an artificial neural network (ANN) architecture. Input features were derived from experimental photocurrent response data, focusing on photocurrent amplitude, decay rates, and persistent levels following UV illumination. Each dataset entry corresponds to a unique wavelength and exposure duration condition, creating a robust classification environment. Our dataset included 300 experimental samples, split into 70 : 30 for training and validation to ensure model robustness. Regularization techniques were applied to prevent overfitting, allowing the ANN model to generalize effectively. As this classification was conducted on experimental data rather than simulated data, the results offer real-world relevance and reliability for future applications.

Data availability

The data that support the findings of this study are available from the corresponding author upon reasonable request.

Conflicts of interest

The authors declare no conflict of interest.

Acknowledgements

This study was supported through the National Research Foundation of Korea [NRF- 2023R1A2C2003242, NRF-2022M3I7A3037878, and RS-2024-00403069] of the Ministry of Science and ICT, Republic of Korea.

References

1 R. E. Neale, P. W. Barnes, T. M. Robson, P. J. Neale, C. E. Williamson, R. G. Zepp, S. R. Wilson, S. Madronich, A. L. Andrady, A. M. Heikkilä, G. H. Bernhard, A. F. Bais, P. J. Aucamp, A. T. Banaszak, J. F. Bornman, L. S. Bruckman, S. N. Byrne, B. Foereid, D. P. Häder, L. M. Hollestein, W. C. Hou, S. Hylander, M. A. K. Jansen, A. R. Klekociuk, J. B. Liley, J. Longstreth, R. M. Lucas, J. Martinez-Abaigar, K. McNeill, C. M. Olsen, K. K. Pandey, L. E. Rhodes, S. A. Robinson, K. C. Rose, T. Schikowski, K. R. Solomon, B. Sulzberger, J. E. Ukpebor, Q. W. Wang, S. Wängberg, C. C. White, S. Yazar, A. R. Young, P. J. Young, L. Zhu and M. Zhu, *Photochem. Photobiol. Sci.*, 2021, **20**, 1–67.

2 E. Reid, T. Igou, Y. Zhao, J. Crittenden, C. H. Huang, P. Westerhoff, B. Rittmann, J. E. Drewes and Y. Chen, *Environ. Sci. Technol.*, 2023, **57**, 7150–7161.

3 H. Chen, K. Liu, L. Hu, A. A. Al-Ghamdi and X. Fang, *Mater. Today*, 2015, **18**, 493–502.

4 B. C. Hodges, E. L. Cates and J. H. Kim, *Nat. Nanotechnol.*, 2018, **13**, 642–650.

5 A. C. Green, S. C. Wallingford and P. McBride, *Prog. Biophys. Mol. Biol.*, 2011, **107**, 349–355.

6 J. Lu, Q. Ye, C. Ma, Z. Zheng, J. Yao and G. Yang, *ACS Nano*, 2022, **16**, 12852–12865.

7 M. Kumar and H. Seo, *Adv. Opt. Mater.*, 2023, **11**(24), 2301165.

8 X. Xu, J. Chen, S. Cai, Z. Long, Y. Zhang, L. Su, S. He, C. Tang, P. Liu, H. Peng and X. Fang, *Adv. Mater.*, 2018, **30**(43), 1803165.

9 E. L. P. Dumont, P. D. Kaplan, C. Do, S. Banerjee, M. Barrer, K. Ezzedine, J. H. Zippin and G. I. Varghese, *Front. Med.*, 2024, **11**, 1259050.

10 H. Lu, J. Xie, X. Y. Wang, Y. Wang, Z. J. Li, K. Diefenbach, Q. J. Pan, Y. Qian, J. Q. Wang, S. Wang and J. Lin, *Nat. Commun.*, 2021, **12**, 2798.

11 T. Li, J. Miao, X. Fu, B. Song, B. Cai, X. Ge, X. Zhou, P. Zhou, X. Wang, D. Jariwala and W. Hu, *Nat. Nanotechnol.*, 2023, **18**, 1303–1310.

12 M. Kumar, J. Lim, S. Kim and H. Seo, *ACS Nano*, 2020, **14**, 14108–14117.

13 L. Mennel, J. Symonowicz, S. Wachter, D. K. Polyushkin, A. J. Molina-Mendoza and T. Mueller, *Nature*, 2020, **579**, 62–66.

14 F. Zhou and Y. Chai, *Nat. Electron.*, 2020, **3**, 664–671.

Open Access Article. Published on 19 November 2024. Downloaded on 07.04.2026 03:05:20.
This article is licensed under a Creative Commons Attribution 3.0 Unported Licence.

15 D. Jayachandran, A. Oberoi, A. Sebastian, T. H. Choudhury, B. Shankar, J. M. Redwing and S. Das, *Nat. Electron.*, 2020, **3**, 646–655.
16 V. K. Sangwan and M. C. Hersam, *Nat. Nanotechnol.*, 2020, **15**, 517–528.
17 X. Chen, Y. Xue, Y. Sun, J. Shen, S. Song, M. Zhu, Z. Song, Z. Cheng and P. Zhou, *Adv. Mater.*, 2022, 2203909.
18 C. Pan, C. Y. Wang, S. J. Liang, Y. Wang, T. Cao, P. Wang, C. Wang, S. Wang, B. Cheng, A. Gao, E. Liu, K. Watanabe, T. Taniguchi and F. Miao, *Nat. Electron.*, 2020, **3**, 383–390.
19 D. Kumar, H. Li, U. K. Das, A. M. Syed and N. El-Atab, *Adv. Mater.*, 2023, **35**(28), 2300446.
20 T. Wan, B. Shao, S. Ma, Y. Zhou, Q. Li and Y. Chai, *Adv. Mater.*, 2023, **35**(37), 2203830.
21 J. Chen, Z. Zhou, B. J. Kim, Y. Zhou, Z. Wang, T. Wan, J. Yan, J. Kang, J. H. Ahn and Y. Chai, *Nat. Nanotechnol.*, 2023, **18**, 882–888.
22 E. Marder and A. L. Taylor, *Nat. Neurosci.*, 2011, **14**, 133–138.
23 A. Neishabouri and A. A. Faisal, *PLoS Comput. Biol.*, 2014, **10**(5), e1003615.
24 C. Århammar, A. Pietzsch, N. Bock, E. Holmström, C. M. Araujo, J. Gråsjö, S. Zhao, S. Green, T. Peery, F. Hennies, S. Amerioun, A. Föhlisch, J. Schlappa, T. Schmitt, V. N. Strocov, G. A. Niklasson, D. C. Wallace, J. E. Rubensson, B. Johansson and R. Ahuja, *Proc. Natl. Acad. Sci. U. S. A.*, 2011, **108**, 6355–6360.
25 S. Y. Lee, J. Kim, A. Park, J. Park and H. Seo, *ACS Nano*, 2017, **11**, 6040–6047.
26 S. Fritz, L. Radtke, R. Schneider, M. Luysberg, M. Weides and D. Gerthsen, *Phys. Rev. Mater.*, 2019, **3**, 114805.
27 M. Weidner, A. Fuchs, T. J. M. Bayer, K. Rachut, P. Schnell, G. K. Deyu and A. Klein, *Adv. Funct. Mater.*, 2019, **29**(14), 1807906.
28 M. J. Spijkman, K. Myny, E. C. P. Smits, P. Heremans, P. W. M. Blom and D. M. De Leeuw, *Adv. Mater.*, 2011, **23**, 3231–3242.
29 E. Fortunato, P. Barquinha and R. Martins, *Adv. Mater.*, 2012, **24**, 2945–2986.
30 M. Kumar and T. Som, *Nanotechnology*, 2015, **26**, 345702.
31 Y. Gao, S. F. Al-Sarawi and D. Abbott, *Nat. Electron.*, 2020, **3**, 81–91.
32 E. J. Fuller, S. T. Keene, A. Melianas, Z. Wang, S. Agarwal, Y. Li, Y. Tuchman, C. D. James, M. J. Marinella, J. J. Yang, A. Salleo and A. A. Talin, *Science*, 2019, **364**, 570–574.
33 M. Kumar, J. Lim and H. Seo, *Nano Energy*, 2021, **89**, 106471.
34 Y. Sharma, J. Balachandran, C. Sohn, J. T. Krogel, P. Ganesh, L. Collins, A. V. Ievlev, Q. Li, X. Gao, N. Balke, O. S. Ovchinnikova, S. V. Kalinin, O. Heinonen and H. N. Lee, *ACS Nano*, 2018, **12**, 7159–7166.
35 A. Mazumder, C. K. Nguyen, T. Aung, M. X. Low, M. A. Rahman, S. P. Russo, S. A. Tawfik, S. Wang, J. Bullock, V. Krishnamurthi, N. Syed, A. Ranjan, A. Zavabeti, I. H. Abidi, X. Guo, Y. Li, T. Ahmed, T. Daeneke, A. Al-Hourani, S. Balendhran and S. Walia, *Adv. Funct. Mater.*, 2023, **33**(36), 2303641.
36 M. Kumar, S. Abbas and J. Kim, *ACS Appl. Mater. Interfaces*, 2018, **10**, 34370–34376.
37 G. Y. Lee, B. S. Mun and H. Ju, *Adv. Electron. Mater.*, 2022, **8**(7), 2101327.
38 W. Xu, H. Cho, Y. H. Kim, Y. T. Kim, C. Wolf, C. G. Park and T. W. Lee, *Adv. Mater.*, 2016, **28**, 5916–5922.
39 T. U. Singh, A. Nandi and R. Ramaswamy, *Phys. Rev. E: Stat., Nonlinear, Soft Matter Phys.*, 2008, **77**, 066217.
40 S. G. Patel, D. D. Kelson, L. E. Abramson, Z. Sattari and B. Lorenz, *Astrophys. J.*, 2023, **945**, 93.